RESEARCH ARTICLE

WILEY

Spatiotemporal variability of streamflow in the Pearl River Basin: Controls of land surface processes and atmospheric impacts

Ying Zhang[1] | Jianping Gan[1] | Qichun Yang[2]

[1]Department of Ocean Science, and Department of Mathematics, Center for Ocean Research in Hong Kong and Macau, Hong Kong University of Science and Technology, Hong Kong, China

[2]Earth, Ocean and Atmospheric Sciences Thrust, Hong Kong University of Science and Technology (Guangzhou), Guangzhou, China

Correspondence
Jianping Gan, Department of Ocean Science, and Department of Mathematics, Center for Ocean Research in Hong Kong and Macau, Hong Kong University of Science and Technology, Hong Kong, China.
Email: magan@ust.hk

Abstract

To advance understanding of the spatiotemporal variability of the streamflow in the Pearl River Basin (PRB), we used the Soil and Water Assessment Tool model to simulate the water fluxes from 2010 to 2020 and to identify the underlying controlling mechanisms. The streamflow in the PRB is highly variable and controlled by complex land surface processes and atmospheric impacts over the heterogeneous terrain. Two key factors primarily govern the streamflow: (1) the location of the active precipitation zone, which is determined by the interaction between the monsoon path and uplifting effect of the terrain, and (2) the redistributions resulting from land use and soil characteristics. We observe distinct patterns in the different water fluxes across the different regions. Specifically, surface flow exhibits the highest activity within the precipitation zone. Lateral flow and actual evapotranspiration (AET) have the greatest intensity in the forests and in agricultural regions, respectively, and the aquifer flow is more active in areas with coarse soil textures. The land surface processes of the AET and aquifer retention significantly govern the temporal variability of the streamflow, contributing to the precipitation and streamflow being out of phase in the PRB. Based on the underlying mechanisms driving streamflow variability, we classify the PRB into three substreams: a drought-prone upstream, a hydrologically active midstream, and a typhoon-affected downstream, and each substream exhibits distinct spatiotemporal characteristics of streamflow. We find that the time series and probability distributions of the streamflow at different tributaries within each substream are similar. Each probability distribution is multimodal and can be decomposed into three unimodal distributions representing dry, transitional, and wet conditions. Specifically, the PRB features a large and steep dry mode, a flat transitional mode, and a short wet mode.

KEYWORDS
hydrological modelling, land surface processes, monsoon climate, spatiotemporal variability, watershed hydrology

1 | INTRODUCTION

The water cycle is crucial in linking the atmosphere-land-ocean continuum, promoting sustainable environment, and ensuring water security (Dai et al., 2018; Veettil & Mishra, 2016). Investigation of large watersheds in monsoon-affected regions is of importance, as they exemplify the characteristics of the monsoon areas that span 25% of the Earth's surface. The spatiotemporal variability of hydrological processes and the underlying mechanisms that regulate the terrestrial water cycle can be complex and not well understood. This lack of understanding hinders effective water resource management and the maintenance of societal well-being (Wu & Xu, 2006; Yamamoto et al., 2019).

Large watersheds are highly heterogeneous, and different parts of basins can exhibit distinct hydrological characteristics across multiple river systems. Previous investigations have commonly relied on topography to delineate subregions within watersheds (Niu, 2010; PRWRC, 2021). While this method recognizes the fundamental role of topography in shaping river networks and water movement, the method often neglects the spatial patterns of other influences, such as precipitation, land use, and soil, which also contribute to hydrological variability. Regionalization based on cluster analysis is an alternate technique for classifying a river basin into various subregions. It is based on the distribution of a specific controlling variable, such as extreme precipitation, drought, or flood events, rather than considering a holistic hydrological perspective (Liu et al., 2021; Yang et al., 2010; Zhang et al., 2012; Zhou et al., 2021). A more effective approach for addressing hydrological heterogeneity is regionalization based on a combination of multiple water components (Knoben et al., 2018; Niu et al., 2017). This method enables the identification of dominant factors that control regional hydrology more effectively. However, it requires abundant high-resolution datasets of hydrological processes.

In contrast to their spatial features, the temporal dynamics of streamflow have been extensively studied using gauge observations, revealing various timescale variabilities such as interannual trends, seasonal variations, and extreme events (Niu et al., 2014; Niu et al., 2017; Zhang et al., 2014). However, these studies primarily relied on scatter point observations, limiting their ability to comprehensively capture streamflow patterns at large spatial scales and to characterize the connections between streams (Yu et al., 2018). These connections are crucial for maintaining ecosystem integrity and for managing water quality. On the other hand, probability distribution functions (PDFs), such as the normal, log-normal, and gamma distributions, are valuable tools for assessing streamflow temporal dynamics (Niu et al., 2015; Shukla & Wood, 2008; Zhang et al., 2009). However, in regions with complex climate zones and land surfaces, these traditional PDFs might not capture the streamflow behaviour adequately due to the presence of multiple peaks resulting from the interactions of multiple factors affecting runoff generation (Niu, 2010). Recently, multimodality theory has emerged as a promising approach for fitting complex distributions and has potential for investigating streamflow with high temporal variability (Bell et al., 2004; Lee et al., 2012; Shanyavskiy & Soldatenkov, 2019).

High variability in the terrestrial water cycle results from the comprehensive effects of regional atmospheric forcing, terrain topography, land use, and soil properties (Ribolzi et al., 2018). Precipitation has substantial spatial and temporal variability, especially in large monsoon zones characterized by distinct wet and dry seasons. Topography, including elevation, distance to the sea, and mountains, affects runoff generation and river routing (Wu et al., 2021). Mountains, for example, often lead to substantial changes in the magnitude of local precipitation and eventually contribute to the spatial heterogeneity of the streamflow. The discharge response depends on the topographic characteristics of a watershed. For instance, fan-shaped basins typically exhibit a quick response of streamflow to precipitation, and broad and flat basins often exhibit the opposite behaviour (Niu, 2010; Wang et al., 2018).

Land surface properties, such as land use, significantly alter precipitation pathways through various processes, including canopy interception, infiltration, and evapotranspiration. Forests and agricultural lands, characterized by extensive leaf coverage, exhibit high evapotranspiration rates, leading to a greater soil water retention (Yan et al., 2018; Yang et al., 2018). Conversely, urban and barren areas promote increased runoff due to impervious surfaces (Giri et al., 2018), while floodplain wetlands contribute to flood mitigation and groundwater replenishment (Bullock & Acreman, 2003).

Soil property is another factor critical for water movement through infiltration and recharge (Gao et al., 2021). A wide range of soil properties, including soil bulk density, porosity, and particle composition, can directly influence water movement and moisture dynamics in the soil profile (Deng et al., 2018). For instance, permeable sandy soils often increase rainwater infiltration and groundwater contribution (Ribolzi et al., 2018). However, it remains unknown which soil property is dominant in regulating water fluxes (Lin, 2012). Furthermore, soil properties vary substantially in space, contributing to the spatial variability of hydrological processes (Bossa et al., 2012).

Understanding the spatiotemporal characteristics of streamflow and the complex interactions between atmospheric forcing and land surface properties remains a challenge. Fortunately, process-based hydrological models provide a viable solution to address this challenge (Arnold et al., 2012; Bieger et al., 2017). These models explicitly simulate critical processes within the terrestrial water cycle, making it possible to quantify the variability of multiple water fluxes and explore the underlying mechanisms (Fu et al., 2019; Ly et al., 2019). One of the most effective hydrological models is the soil and water assessment tool (SWAT), which is flexible in the spatial resolution of simulation units, making it suitable for watershed-scale streamflow, sediment transport, and nutrient cycling studies (Arnold et al., 1998).

In this study, we conducted a comprehensive investigation into the hydrological processes of the Pearl River Basin (PRB), which is characterized by a subtropical monsoon climate and diverse landscapes. Our study aims to achieve the following objectives: (1) investigate the spatiotemporal characteristics of key water fluxes that control the streamflow in the basin, (2) evaluate the interactive impacts of atmosphere-land surface properties on the water cycle in the PRB, and (3) identify land surface processes that regulate

hydrological variability across the heterogeneous nature of subregions. To the best of our knowledge, this study represents the first systematic analysis of the spatiotemporal characteristics of streamflow controlled by highly variable surface processes and atmospheric impacts in the PRB.

2 | METHODS

2.1 | Study area

The Pearl River has an average discharge of 9631 m³/s and is the second-largest river in China in terms of annual streamflow. This water system consists of three main rivers: the West, North, and East Rivers, and they merge into the Pearl River Delta (PRD) and flow into the Pearl River Estuary. The Pearl River covers an area of 4.4×10^5 km² in southern China and has a typical subtropical monsoon climate (Figure 1a). The basin receives annual precipitation ranging from 1200 to 2200 mm/year, with the wet season (April–September) accounting for nearly 80% of the total precipitation (PRWRC, 2021). The annual temperature varies between 14 and 22°C. The PRB has distinct geographic features, including the Yungui Plateau in the northwestern region of the basin, mountains in the northern parts, and plains in the coastal regions. It is home to 124 million people and provides essential societal, ecological, and economic services to the Guangdong-Hong Kong-Macao Greater Bay Area (GBA). Studying the streamflow characteristics and underlying controlling mechanisms in the basin is critical for understanding the
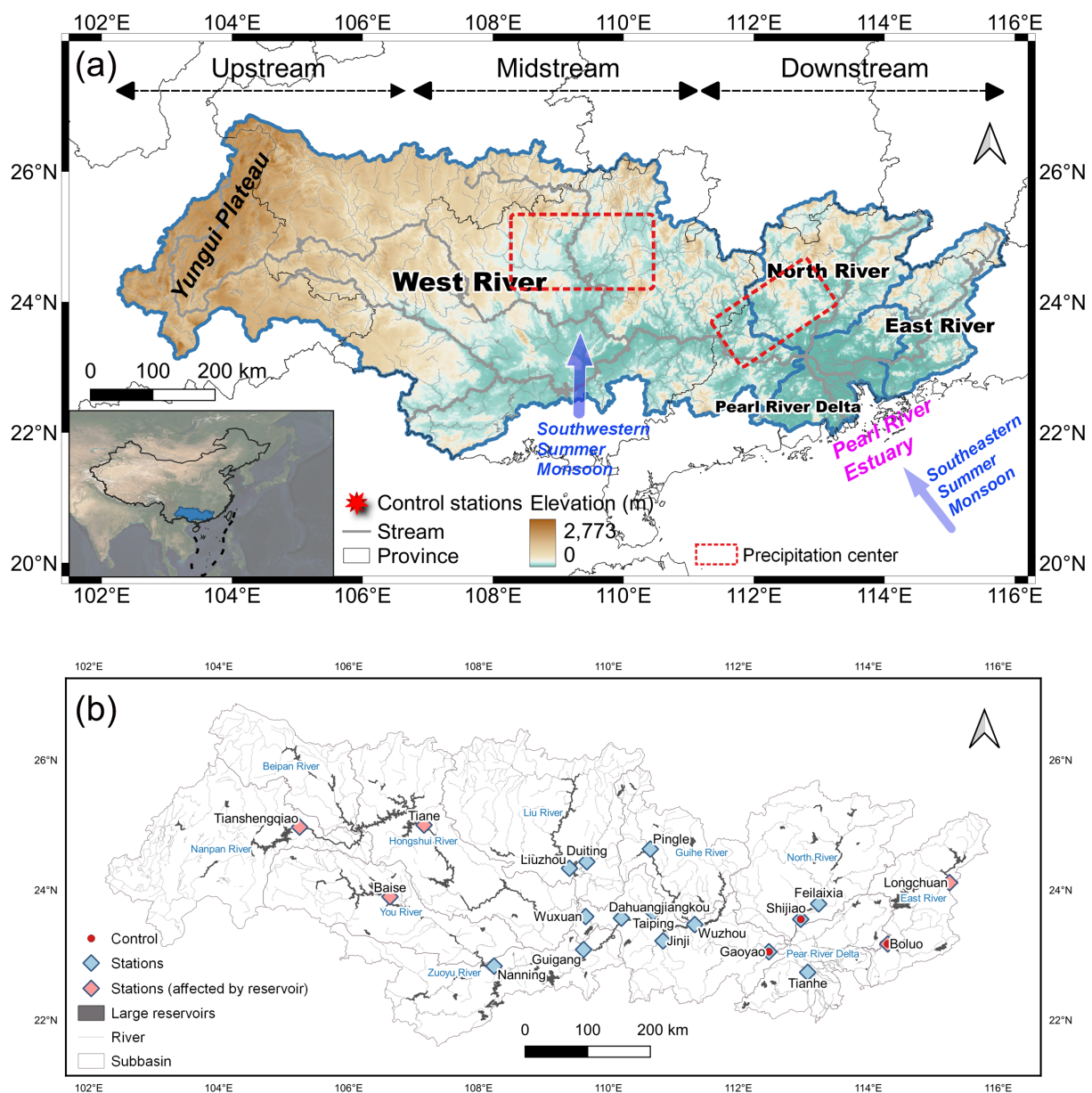

FIGURE 1 Location and topography of the Pearl River Basin, and (b) locations of hydrological stations and large reservoirs.

frequent extreme floods and droughts in the region and the freshwater discharge into the adjacent coastal ocean.

2.2 | The SWAT model

2.2.1 | Model description

We utilized the SWAT model (SWAT+ version) to simulate and study the hydrological processes in the PRB. The model employs Hydrological Response Units (HRUs) as the computation unit, which account for the heterogeneity of landscapes based on a combination of terrain, soil, land use, and management (Arnold et al., 2012; Wu et al., 2023). The model is composed of two phases: a land phase based on HRUs, and a stream phase simulating water movements in channels. The simulations are conducted on a daily scale. The simulation of key water fluxes in SWAT is summarized in Equations (1)–(3) and depicted in Figure 2.

$$Q_{tot} = Q_{sur} + Q_{lat} + Q_{aqu}, \tag{1}$$

$$Q_{sur} + Q_{lat} = Precip - AET - Perc - \Delta Sw, \tag{2}$$

$$Q_{aqu} = Rchrg - Revap - Seep_{deep} - \Delta Aq_{stor,} \tag{3}$$

where Q_{tot}, Q_{sur}, Q_{lat}, and Q_{aqu} represent the total flow, surface flow, lateral flow, and aquifer flow, respectively. Precip denotes precipitation, and Perc stands for percolation from the root zone into the vadose zone. Rchrg, Revap, and $Seep_{deep}$ represent water entering the aquifer from the root zone, re-evaporation from the shallow aquifer into the overlying root zone, and seepage from the shallow to the deep aquifer, respectively. Furthermore, ΔSW and ΔAq_{stor} represent the changes in water storage in the root zone and shallow aquifer, respectively. All the terms are in millimetre (mm) units. More details of SWAT+ can be found in Bieger et al. (2017).

2.2.2 | Datasets for SWAT simulation

Table 1 lists all the datasets we used in this study to drive the SWAT model and perform validation and uncertainty analysis of the simulations. We utilized soil, topography, and land use maps collected from the National Cryosphere Desert Data Center to set up the model. For weather data, we employed the meteorological dataset AgrEra5, which spans from January 2007 to December 2020 and is downscaled from the hourly ECMWF ERA5 data to a spatial resolution of 0.1°. To assess the quality of this dataset, we compared it with 53 NOAA weather stations and two reanalysis datasets: CFSR and CMADS for the PRB between 2008 and 2014. This period corresponds to a time when all four datasets are available.

Our findings reveal that AgrEra5 outperforms other reanalysis datasets when integrated with our SWAT model, as evidenced by its highest correlation coefficient (r), deterministic coefficient (R^2), and the lowest root mean square error (RMSE) for most meteorological parameters, except for wind speed (Table S1 and Figure S1). Regarding solar radiation, given the limited availability of observations, we compared the meteorological reanalysis datasets with the ISCCP, a global surface solar radiation dataset. AgrEra5 shows superior performance in both temporal ($R^2 = 0.87$, RMSE = 1.8) and spatial patterns (Figures S2 and S3), outperforming CFSR and CMADS. However, it is important to note a particular limitation concerning the precipitation data: after removing zero values and missing observations, AgrEra5
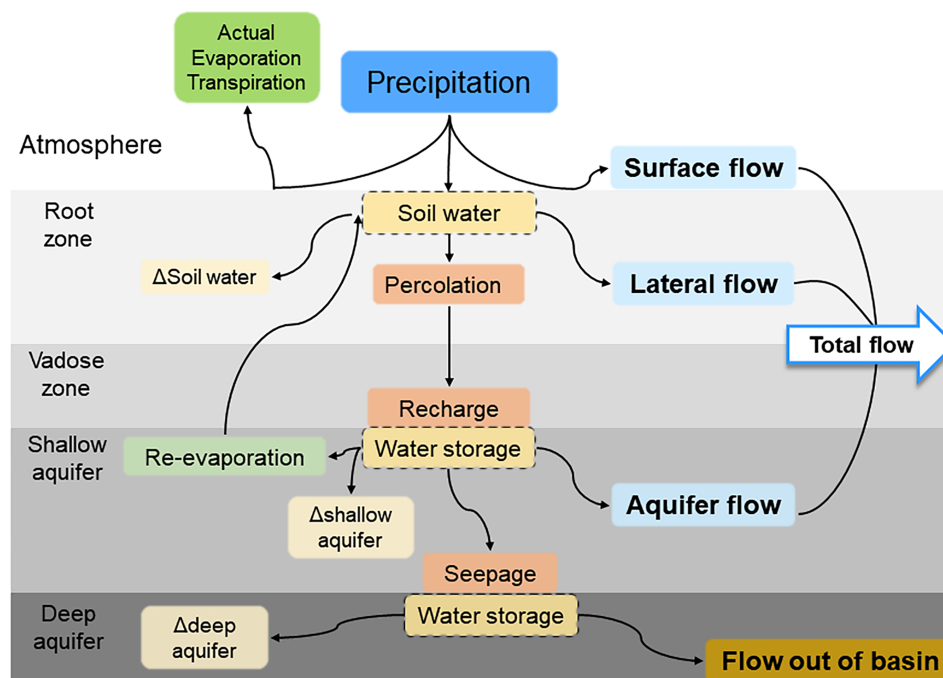
FIGURE 2 Schematic of the soil and water assessment tool (SWAT) model representing hydrological processes and pathways within one Hydrological Response Unit (HRU).

TABLE 1 Datasets to drive the soil and water assessment tool (SWAT) and perform validation and uncertainty analysis of the simulations.

Function	Dataset		Period	Domain	Resolution		Source
	Abbreviation	Full name/ description			Time	Spatial	
Geography maps to set up SWAT	–	Chinese soil dataset based on the World Soil Database (HWSD) (v1.1)	2009	China	Static	~0.009° (1 km)	http://www.ncdc.ac.cn/portal/metadata/a948627d-4b71-4f68-b1b6-fe02e302af09
	–	Data set of 1 km resolution DEM in China	2019	China	Static	~0.009° (1 km)	http://www.ncdc.ac.cn/portal/metadata/ba0e4b6b-8fef-4eec-9c84-81646f266282
	–	GLC_FCS30: global land-cover product with fine classification system at 30 m using time-series Landsat imagery	2020	China	Static	~0.009° (1 km)	https://data.casearth.cn/sdo/detail/5fbc7904819aec1ea2dd7061
Validation of forcing dataset	AgrEra5	Global Weather for Agriculture based on the hourly ECMWF ERA5 data	1979–present	Global	Daily	0.1°	https://cds.climate.copernicus.eu/cdsapp#!/dataset/sis-agrometeorological-indicators?tab=overview
	CMADS	China Meteorological Assimilation Driving Datasets for the SWAT model (version: v1.2)	2008–2018	East Asia	Daily	0.125°	https://cmads.org/
	CFSR	Climate Forecast System Reanalysis	1979–2017	Global	Daily	0.3125°	https://climatedataguide.ucar.edu/climate-data/climate-forecast-system-reanalysis-cfsr
Precipitation	GPM	Global Precipitation Measurement (version: 3IMERGDF.06)	2000–present	Global	Daily	0.1°	https://gpm1.gesdisc.eosdis.nasa.gov/data/GPM_L3/GPM_3IMERGDF.06/
Solar radiation	ISCCP	Dataset of high-resolution (3 hour, 10 km) global surface solar radiation	1983–2018	Global	Up to 3 h	~0.009° (1 km)	http://poles.tpdc.ac.cn/zh-hans/data/be562de3-6367-402f-956d-59ff7c21ad294/
Climate variables except solar radiation	NOAA	Global Hourly—Integrated Surface Database	–	Global	Hourly	Stations	https://www.ncei.noaa.gov/access/data-search/global-hourly
Solar radiation	–	King's Park station of Hong Kong Observatory	1992–present	1 station	Daily	Station	Not open to the public
Validation of SWAT simulation	CAET	Terrestrial evapotranspiration dataset across China	1982–2017	China	Monthly	0.1°	http://poles.tpdc.ac.cn/zh-hans/data/b6d9f525-5b76-48b0-82db-bb2963465cac/
	GREA	A harmonized global land evaporation dataset from model-based products covering 1980–2017	1980–2017	Global	Daily	0.25°	http://poles.tpdc.ac.cn/zh-hans/data/25f7ad68-f98a-41d7-acb7-6b8e19cadc9a/
	GETM			Global	Monthly	~0.009° (1 km)	

(Continues)

TABLE 1 (Continued)

Function	Dataset			Domain	Resolution		Source
	Abbreviation	Full name/ description	Period		Time	Spatial	
		ETMonitor Global Actual Evapotranspiration Dataset with 1-km Resolution	2000–2019				http://poles.tpdc.ac.cn/zh-hans/data/c284bd88-7694-4577-9cbb-02684bd940ff/?q=
PET	CPET	1 km monthly potential evapotranspiration dataset in China	1990–2021	China	Monthly	~0.009° (1 km)	http://poles.tpdc.ac.cn/zh-hans/data/8b11da09-1a40-4014-bd3d-2b86e6dccad4/
Streamflow	Hydrobook	China Hydrological Yearbook	2010–2020	China	Daily	Stations	Not open to the public
	WAPABA	A conceptual monthly rainfall-runoff model	1954–2022	PRB	Monthly	Basin scale	Personal communication
	GloFAS-ERA5	Global Flood Awareness System	1979–2020	Global	Daily	0.1°	https://www.globalfloods.eu/
	GRFR	Global reach-level flood reanalysis (version: V1.0)	1979–2019	Global	Daily	0.05°	https://www.reachhydro.org/home/records/grfr
	CNRD	China Natural Runoff Dataset version 1.0	1961–2018	China	Daily	0.25°	https://poles.tpdc.ac.cn/zh-hans/data/8b6a12c7-c8f9-465a-b449-852fbff51853/
Reservoir affecting streamflow	CRD	China Reservoir Dataset	2022	China	Static	Locations of construction	https://www.scidb.cn/s/zqlFVr
Baseflow index	GSCD	Global Streamflow Characteristics Dataset	2015	Global	Static	0.125°	https://www.gloh2o.org/gscd/

has a low R^2 and a high RMSE (0.31 and 12.56, respectively). Moreover, when compared with the Global Precipitation Measurement dataset, AgrEra5 underestimates precipitation in the coastal regions of Guangdong province (Figure S4). These results indicate the credibility of AgrEra5 as a reliable resource for hydrological studies in the PRB; however, they also highlight its limitations.

To calibrate and validate the model, we obtained daily streamflow data from 19-gauge stations spanning the years 2010–2020, ensuring comprehensive representation of each mainstream of the Pearl River with at least one station (Figure 1b). These data were sourced from the China Hydrological Yearbook. However, it should be noted that the streamflow patterns at five upstream stations are affected by large reservoirs. To demonstrate the significant impact of these reservoirs, we calculated the residence time, defined as the reservoir's water storage capacity divided by its annual discharge. The residence time for the five hydrological stations is all above 0.3 years (Table S2).

The study area comprised five land use types and 45 soil types, and we assumed static land use and soil properties throughout the study period. We delineated HRUs using thresholds of 17% for land use, 14% for soil, and 18% for slope. Additionally, we merged small HRUs into larger ones with similar landscape features. These threshold values are based on our model assessment and aim to maintain a balance between computation costs and model resolution. Furthermore, we verified that the defined land use and soil of HRUs were consistent with the corresponding raster file. Overall, the model comprises 201 subbasins and 4679 HRUs.

2.2.3 | Model calibration and validation

We utilized periods of 3 years (2007–2009), 5 years (2010–2014), and 6 years (2015–2020) for model spin-up, calibration, and validation, respectively. During the calibration and validation processes, we utilized data from three control gauge stations: Gaoyao on the West River, Shijiao on the North River, and Boluo on the East River, respectively (Figure 1). These stations were chosen as control points because they are located at the confluence of rivers in the lower reaches of the PRD plain, which forms a network of interconnected rivers. Moreover, these stations are positioned away from the tidal effects of the Pearl River Estuary. In addition to the main calibration and validation at these three stations, we further evaluated the model simulations using data from an additional 16 hydrological stations (Figure 1b). To evaluate the performance of the baseflow simulation, we used the baseflow separation method proposed by Eckhardt (2005) to derive baseflow from the time series of streamflow observations and simulations.

To calibrate and validate the model, we selected three common metrics evaluation (Moriasi et al., 2007), including RMSE-observations standard deviation ratio (RSR), Nash-Sutcliffe efficiency (NSE), and percent bias (Pbias) (Equation S1). We identified the sensitive parameters from the literature (Ren et al., 2022; Shuler et al., 2020; Zeiger et al., 2021; Zhang et al., 2020) and evaluated their sensitivity to streamflow patterns using the SWAT+ Toolbox, a tool for sensitivity

analyses and calibration. After filtering the parameters, we manually adjusted them (Table 2) to align with the streamflow patterns, such as baseflow and peaks, so that the total flow matched observations within the criteria of the three metrics (Table S3).

2.3 | Statistical analysis of streamflow

2.3.1 | Temporal patterns of streamflow PDFs

We used the multimodality of PDFs to describe the combination of subordinate normal distributions for the temporal pattern in the streamflow. We employed curve fitting analysis to decompose a multimodal streamflow PDF into three subordinate normal PDFs:

$$P = \sum_{i=1}^{3} \frac{P_i}{\sqrt{2\pi}\sigma_i} \exp\left[-\left(\frac{S-S_i}{2\sigma_i}\right)^2\right] \times 100\%, \quad (4)$$

where S and P are the streamflow value (m^3/s) and corresponding normalized probability (%), respectively, and P_i, S_i, and σ_i are the representative probability (%), centre streamflow value (m^3/s), and standard deviation of the ith unimodal PDF (m^3/s), respectively. Because their central values increase in sequence, we interpreted the three PDFs as dry, transitional, and wet modes.

To judge the quality of the fit, we used the sum of errors (S_E) between the raw ($S_{raw,i}$) and fitted data ($S_{fit,i}$):

$$S_E = \sum_{i=1}^{n} |S_{fit,i} - S_{raw,i}| \times 100\%. \quad (5)$$

### 2.3.2 | Analysis of streamflow characteristics

The basin analysis, based on spatial patterns of water fluxes, revealed the division of the PRB into three distinct subregions, referred to as "substreams": the upstream region (longitude 102° to 106.5°E), midstream region (106.5° to 111° E), and downstream region (111°–116°E) (Figure 1a). We conducted an in-depth analysis of the spatiotemporal characteristics of the streamflow within these substreams.

We utilized the Strahler stream system (Strahler, 1957) to identify the orders of the river channels in the watershed. This system concisely represents river networks by assigning a hierarchy to the streams that starts from the outermost tributary (order = 1) to the mainstream (highest order) (Sah & Das, 2017; Tarboton et al., 1991). The total number of channels was 461 in the PRB, with 195, 152, 60, 41, and 13 channels of orders 1–5, respectively.

In addition, we calculated the runoff coefficient η, representing the ratio of runoff to precipitation, as an indicator of water retention on the land surface. In assessing the spatial/temporal variability of the flow, we employed the coefficient of variation (c_v) as a measure of data dispersion around the mean value, which is defined as the ratio of the standard deviation σ to the mean μ, expressed as $c_v = \sigma/\mu$.

TABLE 2 Calibrated parameters in the soil and water assessment tool.

Parameter	File	Level	Calibrated	Range	Default	Description
perco	hydrology.hyd	HRU	0.97	0–1	1	Percolation coefficient
latq_co	hydrology.hyd	HRU	40	–	1	Plant ET curve number coefficient
cn3_swf	hydrology.hyd	HRU	0.4	0–1	0	Soil water at cn3
alpha_bf	aquifer.aqu	Subbasin	0.005	0–1	0.048	Alpha factor for groundwater recession curve
dorm_hr	parameters.bsn	Basin	3	0–24	0	Time threshold used to define dormancy
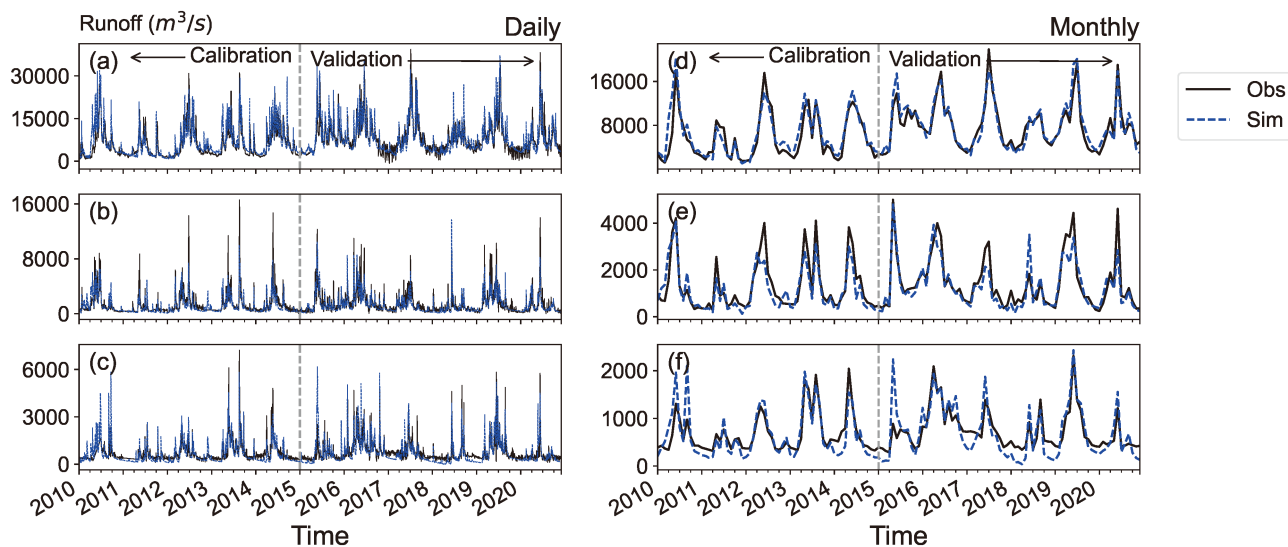
FIGURE 3 Simulated and observed streamflow at the three control gauge stations: (a,d) Gaoyao, (b,e) Shijiao, and (c,f) Boluo stations on a daily (left panels) and monthly (right panels) basis for the calibration (2010–2014) and validation (2015–2020) periods. Obs (solid lines) and Sim (dashed lines) refer to observations and simulated results, respectively.

3 | RESULTS

3.1 | Model performance

Figure 3 illustrates the alignment between our simulated streamflow and observed data at the three control stations, effectively capturing temporal variability. During the calibrations, the daily and monthly *NSE* for the sum of the three stations scores were 0.58 and 0.82, respectively, while validation scores improved to 0.62 and 0.88 (Table 3). The daily and monthly *RSR* during the calibration period were 0.65 and 0.42, with a marginal improvement during validation to 0.63 and 0.35. Additionally, *Pbias* for daily and monthly flows remained below 12%, indicating accurate simulations. The baseflow coefficients were comparable, if not superior, to those for total flow. All of them met or exceeded the 'satisfactory' criteria according to Moriasi et al. (2007)'s performance criteria.

In addition, we evaluated 14 individual normal stations, referring to Tables S4 and S5, and to Figures S5 and S6. On a daily scale for total flow, eight stations met 'satisfactory' performance standards. Regarding baseflow, 12 stations met the 'satisfactory' standards, with two stations being rated as 'very good'. Monthly evaluations displayed a marked improvement, with six stations rated 'very good' for

total flow and five for baseflow. We also analysed the five stations influenced by large reservoirs on an annual scale (Table S6; Figures S7 and S8), all of which achieved a 'satisfactory' performance or higher for total flow. The baseflow coefficients at these stations mirrored those for total flow. Overall, these metrics demonstrate the reliability of the streamflow simulations for our hydrological study.

3.2 | Spatial patterns of water fluxes

Figure 4 illustrates the significant spatial variability of each water flux in the PRB. Precipitation is unevenly distributed across the basin, with the highest amounts (2400 mm/year) occurring in the midstream and decreasing to around 1200 mm/year in the upstream subregion (Figure 4d). On average, 45% of the total precipitation (1810 mm/year) eventually becomes streamflow, and the remaining is mainly consumed by actual evapotranspiration (AET) (52%). The different flow components, including surface flow, lateral flow, and aquifer flow (Equation 1), contribute 24%, 37%, and 39% to the total streamflow, respectively. Surface flow is active in areas with high precipitation, particularly in the midstream region, where values reach up to 500 mm/year and extend towards the delta downstream (Figure 4a).

TABLE 3 Statistical performance of simulated streamflow for the Pearl River Basin (sum of values from the three control stations).

Period	Streamflow	Scale	NSE	RSR	Pbias	Rank
Whole period	Total flow	Daily	0.61	0.62	−8.18	S
		Monthly	0.86	0.37	−8.2	VG
	Baseflow	Daily	0.81	0.44	−9.71	VG
		Monthly	0.86	0.37	−9.74	VG
Calibration	Total flow	Daily	0.58	0.65	−11.7	S
		Monthly	0.82	0.42	−11.79	G
	Baseflow	Daily	0.79	0.45	−10.36	G
		Monthly	0.85	0.39	−10.41	G
Validation	Total flow	Daily	0.62	0.62	−5.92	S
		Monthly	0.88	0.35	−5.91	VG
	Baseflow	Daily	0.8	0.44	−9.28	VG
		Monthly	0.86	0.37	−9.3	VG

Note: The abbreviations VG, G, and S stand for the ranks of Very Good, Good, and Satisfactory, respectively.
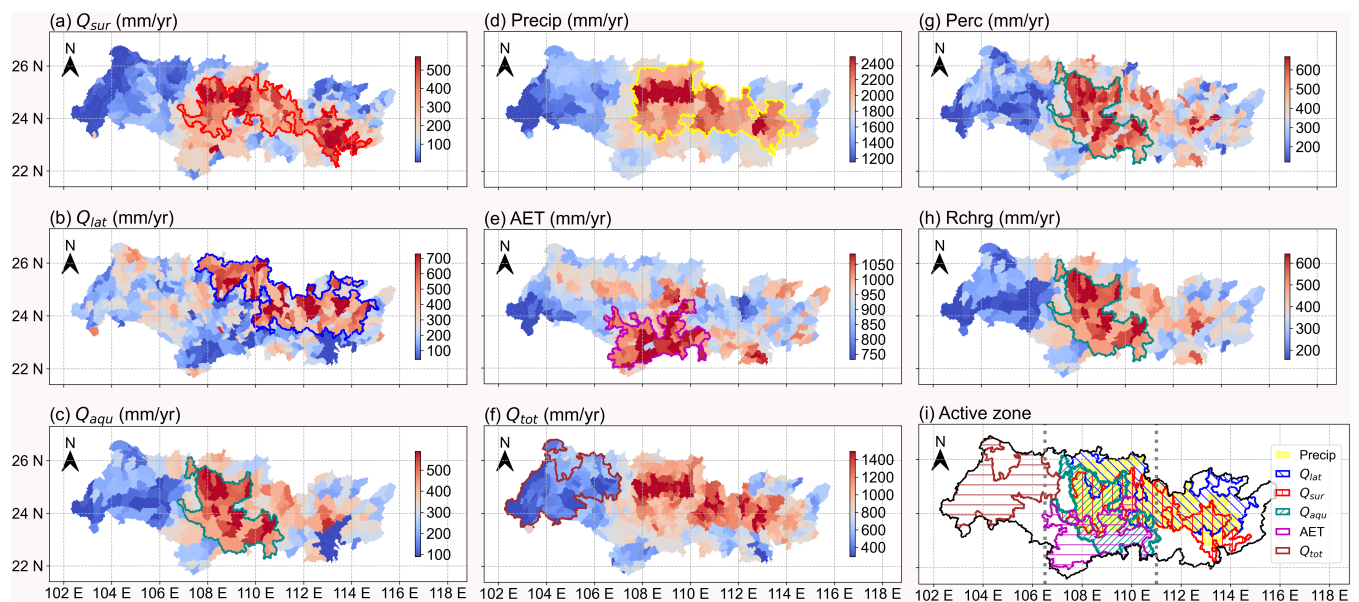

FIGURE 4 Spatial distributions of key water fluxes: (a) surface flow (Q_{sur}), (b) lateral flow (Q_{lat}), (c) aquifer flow (Q_{aqu}), (d) precipitation (Precip), (e) actual evapotranspiration (AET), (f) total flow (Q_{tot}), (g) percolation (Perc), (h) recharge to shallow aquifer (Rchrg), and (i) summary of active zones. Coloured polygons correspond to the active zones of water fluxes in subplots (a)–(h).

In contrast, surface flow is less than 100 mm/year in the inland upstream subregion. Lateral flow is active in the northern part of the PRB, with values exceeding 600 mm/year, but it is relatively inactive in the coastal downstream, where it remains below 100 mm/year (Figure 4b). The active zone of the aquifer flow is in the mid-south part of the midstream subregion (Figure 4c). Overall, the spatial pattern of the total flow, contributed by the surface and baseflows, closely resembles the spatial pattern of the precipitation (Figure 4d,f), indicating the precipitation predominantly contributes to the streamflow in the basin.

AET is most active in the southern areas of the midstream region, suggesting a joint influence of solar radiation and regional land use

(Figure 4e). The annual water fluxes through percolation and groundwater recharge display a pattern like that of the aquifer flow (Figure 4c,g,h), indicating strong retention of water from the root zone into the aquifer layer. The soil water changes in Equation (2) and other residual terms in Equation (3), such as re-evaporation, seepage to the deep aquifer, and aquifer storage change, are minor terms, with values within ±80 mm/year.

In summary (Figure 4i), the upstream, located in the Yungui Plateau, has low streamflow and is a relatively hydrologically dry subregion. The midstream subregion is hydrologically active, where high values of multiple water fluxes intersect, including precipitation, AET, surface, lateral flow, and aquifer flow. The downstream subregion is

close to the coastal margins and consists of the lower reaches of the West, North, and East Rivers. The diverse spatial patterns of the water fluxes indicate the combined influence of external forcing, such as precipitation and solar radiation, and internal processes related to terrain and surface conditions on hydrological processes in the PRB. Consequently, each flow component exhibits its unique active zone across the basin. We analyse and discuss these controlling factors further in Section 4.1.

To further examine the spatial variability of the hydrological processes in the PRB, we zonally averaged the water flux components (Figure 5). The total flow consistently exhibits higher values in the midstream subregion (2.83 mm/day) throughout the year compared to the upstream and downstream subregions (1.23 and 2.5 mm/day, Figure 5a). This distribution aligns with the active zones of precipitation and total flow in the midstream (Figure 4d,f), highlighting their critical roles in water resources management. In contrast, the upstream subregion is characterized as a relatively dry area with lower water availability. This is evident from the lower runoff coefficient η of 32% in this area, much smaller than the 50% in the other two substreams (Figure 5a). The distribution of the aquifer flow follows a pattern like the total flow, but with peaks that shift westward (from 109° to 108°E), suggesting that infiltration processes redistribute the water. Regions with higher lateral flows (at 104°–106° and 110° to 112°E) cover broader longitudes compared to regions with higher surface flows (108° to 110° and 113°–114°E), coinciding with the narrower shapes of the active zones of the surface flow compared to the other flow components (Figures 4, 5a).

3.3 | Temporal patterns of water fluxes

The PRB exhibits a typical monsoon climate characterized by distinct dry and wet seasons, as illustrated in Figures 5c–f. During the wet season (April to September), the three components of the streamflow (surface, lateral, and aquifer flows) exhibit relatively equal magnitudes in the midstream subregion (Figure 5c). However, in the upstream subregion, the lateral flow (1 mm/day) is three times higher than the surface and aquifer flows (both 0.3 mm/day). In the downstream subregion, the lateral flow surpasses the surface and aquifer flows, with values of 1.6, 1.14, and 0.86 mm/day, respectively. These differences indicate distinct flow pathways in each substream.

During the dry season (October to March of the following year), the total streamflow decreases to half of that observed during the wet season (1.4 and 2.95 mm/day, respectively). Notably, the aquifer flow dominates during this period, accounting for 63% of the total flow (Figure 5e). Additionally, the ratio of AET to precipitation reaches almost 100% in the upstream subregion (Figure 5f), indicating rapid depletion of water storage and increased vulnerability to water scarcity in that area. In contrast, the lower substreams exhibit higher water availability, with an AET-to-precipitation ratio of 59%.

To further analyse the spatiotemporal variability, we calculated the monthly water fluxes in each substream (Figure 6). The temporal patterns of water fluxes in the three substreams differed in terms of both magnitude and timing of peaks. Precipitation, total flow, surface flow, and recharge exhibit a consistent trend, with their highest values occurring in early summer (from May to June) in the midstream and downstream subregions, and slightly later from June to September in the upstream subregion. The midstream, which is hydrologically active, consistently demonstrates the highest water values for most water fluxes, except for lateral flow, which is more active in the downstream subregion. Conversely, the drought-prone upstream subregion generally exhibits lower water fluxes each month, except for AET, which aligns with the distribution of precipitation in the PRB.

Among the different water components, the surface flow is the most variable, with a coefficient of variation (c_v) of 0.9 (Figure 6), indicating that the surface flow is sensitive to precipitation. Lateral flow
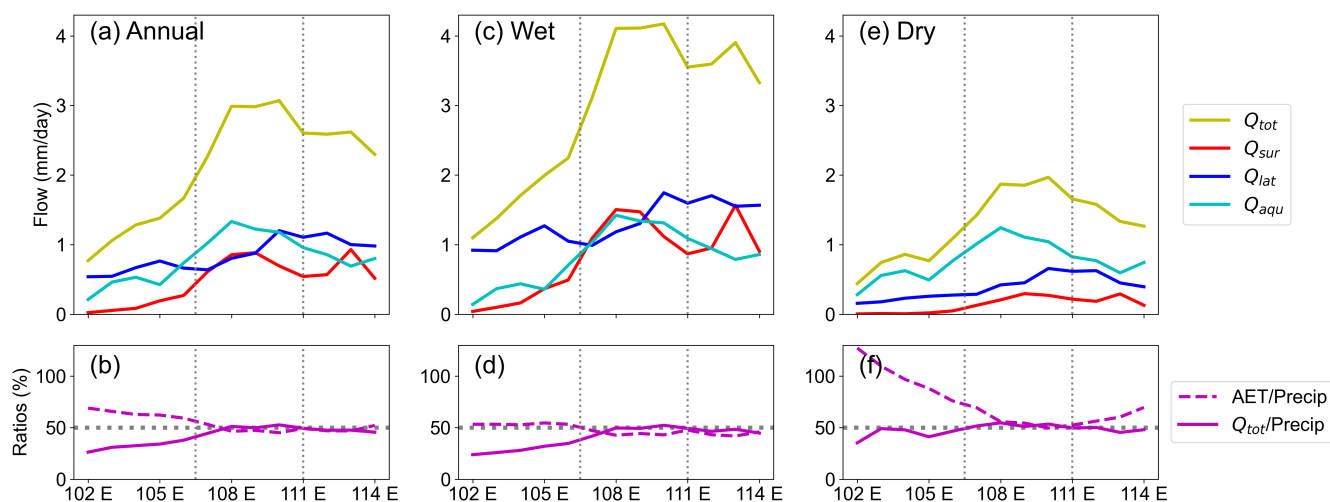

FIGURE 5 Zonally averaged water fluxes: (a,c,e) flow components of total flow (Q_{tot}), surface flow (Q_{sur}), lateral flow (Q_{lat}), and aquifer flow (Q_{aqu}), and (b,d,f) ratios of AET and Q_{tot} to precipitation. The left, centre, and right panels represent the average scale for annual, wet (April–September), and dry seasons (October to next March), respectively.

FIGURE 6 Normalized monthly water fluxes in the three substreams, with the minimum and maximum values annotated on each panel. The fluxes include precipitation (Precip), actual evapotranspiration (AET), the total flow (Q_{tot}), surface flow (Q_{sur}), lateral flow (Q_{lat}), and aquifer flow (Q_{aqu}), and recharge to the shallow aquifer (Rchrg) (from bottom to top panels) in the upstream, midstream, and downstream.
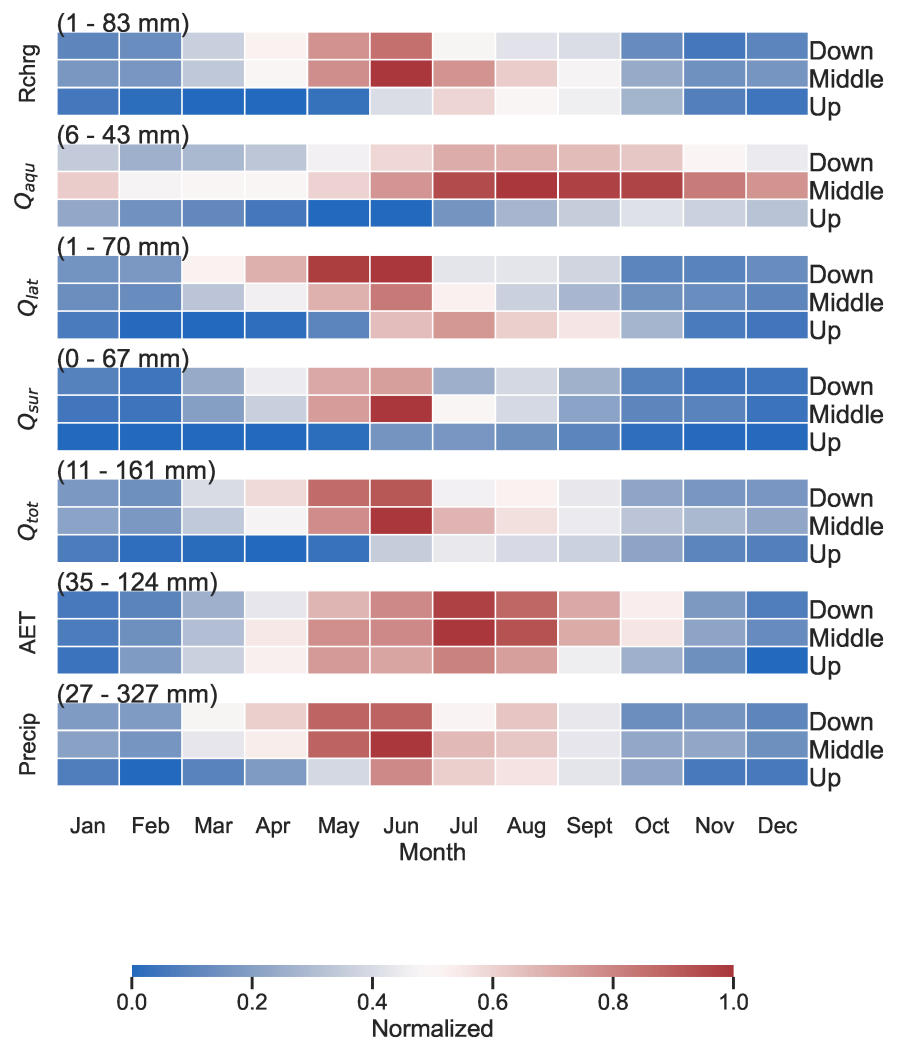
and recharge have similar levels of temporal variability, both have a c_v of 0.77. Precipitation and the total flow comparably variable, both have a c_v of 0.55. In contrast, AET and the aquifer flow have relatively lower variability, with c_v values below 0.35. AET peaks from May to September, and the aquifer flow peaks from July to October. Despite the similar spatial distribution between the recharge and the aquifer flow, with a correlation coefficient (r) of 0.95 (Figure 4c, h), there is a clear time lag and extension between these two variables indicating buffering by soil moisture. Consequently, the behaviour of AET and the aquifer flow contributes to an out-of-phase relationship between precipitation and streamflow in the PRB, highlighting their significance in modulating the hydrological response in the region.

We then analysed the temporal patterns of the surface flow, lateral flow, and aquifer flow at a daily scale for each substream in detail (Figure 7). The aquifer flow is minimally variable throughout the year, indicating its steady contribution as the baseflow. In contrast, the surface flow has large day-to-day variability, while the lateral flow has intermediate levels of variability between the surface and aquifer flows, highlighting their distinct responses to climate events.

The drought-prone upstream subregion accounts for only 14% of the outlet discharge (Figure 7a). The streamflow has the strongest

seasonality in the substream with extremely low values from February to April during the dry season. The aquifer flow dominates the upstream subregion compensating for the reduced surface flow during this period. In June, the streamflow substantially increases primarily because of the lateral flow.

The hydrologically active upstream subregion contributes half of the overall discharge to the adjacent estuary (Figure 7b). We primarily attribute the peak values in the midstream subregion to the surface flow. The downstream subregion streamflow exhibits two distinct peaks (Figure 7b,c). A major peak occurs during mid-June, coinciding with the monsoon season, while a minor peak is observed during mid-August, aligning with the typhoon season. These differences highlight the significance of subregional heterogeneity in shaping the discharge to the coastal ocean.

3.4 | Hydrological variability by river orders

To understand the connections within the substream, we investigated the daily streamflow dynamics across different channel orders (Figure 8). Within each substream, we observe a coherent temporal
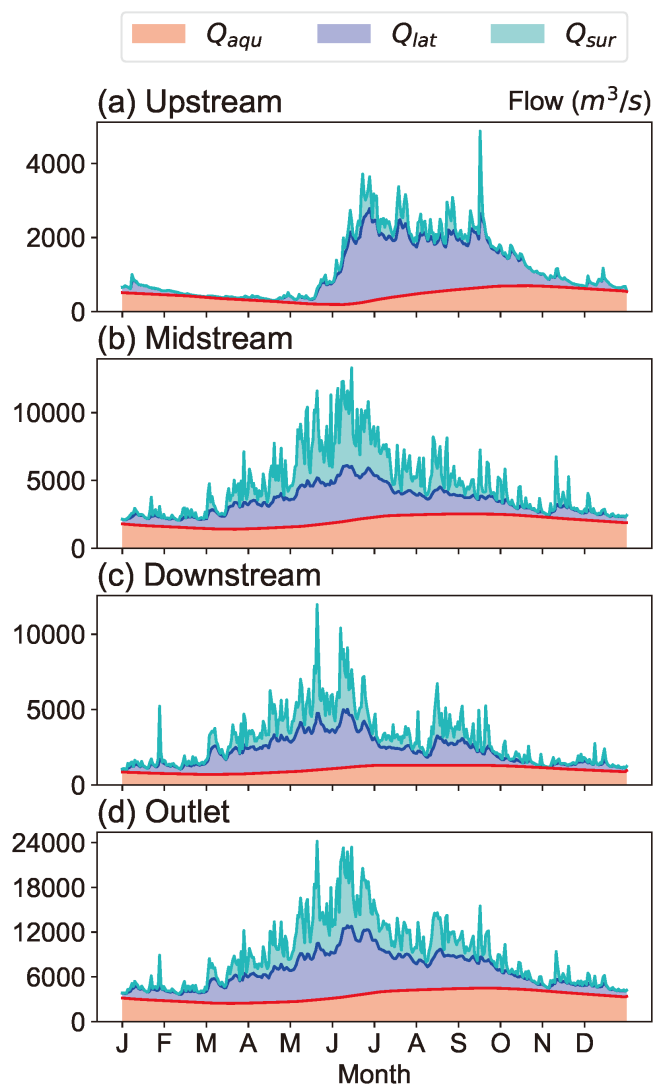
FIGURE 7 Streamflow components in the (a) upstream, (b) midstream, (c) downstream, and (d) basin outlet.

behaviour in the streamflow across different river orders, as evidenced by a high mean inter-correlation ($\bar{r} = 0.94$) among them (Figures 8c–e). These behavioural patterns are similar to the corresponding overall streamflow of each substream (Figures 7, 8), suggesting a relatively stable relationship among flow components within each substream throughout the river network. Furthermore, the streamflow follows a logarithmic growth pattern within each substream that increases from the headwater tributaries with orders of magnitude $O(10^0)$ to the main stream with $O(10^3)$, reflecting the accumulation of streamflow as the rivers progress downstream. Specifically, the midstream and downstream subregions display similar streamflow values for the headwaters, at approximately $14 \, \text{m}^3/\text{s}$ (Figure 8b). However, the streamflow in the hydrologically active midstream has a faster growth rate, reaching $1440 \, \text{m}^3/\text{s}$ at order 4, which is about 60% higher than that of the downstream subregion.

To describe the statistical patterns of the streamflow over time in the PRB, we analysed the PDFs of the streamflow across channel

orders within each substream (Figure 9 and Table 4). The analysis of the overall streamflow in the PRB reveals a large and steep dry mode ($\bar{P} = 51\%$ in Equation 4), a relatively flat transitional mode ($\bar{\sigma} = 267 \, \text{m}^3/\text{s}$), and a short wet mode ($\bar{P} = 9\%$) (Table 4). These modes demonstrate varying contributions across the substreams, reflecting the diverse dynamics of the water resource within each substream (Figure 9). The upstream subregion has a minimal contribution from the wet mode (2%) and a dominant dry mode (58%), indicating its vulnerability to water scarcity. In the midstream subregion, the dry and wet modes exhibit significant probabilities, indicating the strong influence of the monsoon climate. In comparison, the downstream subregion has a lower probability of the dry mode but a higher probability of the transitional mode. For example, for order 5 rivers in the downstream, the transitional mode accounts for almost half of the total probability (48%), indicating a long duration of normal water resources without extreme events.

To evaluate the performance of the fitting method, we compared the multimodal distribution with the unimodal, gamma, and log-normal distributions. The S_E (Equation 5) for these distributions is 27%, 56%, 41%, and 66%, respectively, supporting the superior performance of our method in capturing the temporal features of streamflow. In addition, our fitting method is advantageous because it provides comprehensive information about the duration, centre values, and variability of dry, transitional, and wet conditions. This information is useful for assessing the dynamics of water resources. The method utilization is also flexible in terms of time requirements, as it only necessitates coverage of the entire year.

3.5 | Controls on streamflow

The land surface processes and regional land-atmosphere interaction control the spatiotemporal variability of the streamflow in the PRB. The spatial maps of topography, land use, soil, and precipitation presented in Figure 10 are linked to the active zones of the water fluxes in Figure 4. The local distribution of precipitation is influenced by the terrain topography, leading to a general decrease in precipitation with increasing distance from the coastal area (Figure 10a,d). The plains and hills allow water vapour to travel from the bay and coastal waters inland, creating an active precipitation zone in the PRB. In contrast, the high elevation (>1600 m) of the Yungui Plateau in the upstream region acts as a barrier, blocking the movement of warm and moist air to the headwaters of the West River, resulting in lower precipitation in this region. The precipitation pattern links to the active zones of other water fluxes (Figure 4) and plays a fundamental role in shaping the hydrological processes in the PRB.

Land surface properties, such as land use and soil properties, impact the redistribution among different water components. Agricultural land, for instance, experiences higher AET due to increased transpiration for crop growth (Figures 4e, 10b). Forested regions, on the other hand, have active lateral flow due to their high percolation rates (Figures 4b, 10b). Areas with extensive impervious surfaces, such as the PRD, tend to convert most of the precipitation into surface flow

FIGURE 8 (a) Distributions of river channel orders, (b) runoff at stream orders 1 and 4 in the three substreams, and runoff of different orders of channels within each substream for (c) the upstream, (d) midstream, and (e) downstream. The bottom to top lines in subplots (c) to (e) correspond to increasing hierarchical stream orders from 1 to 5.
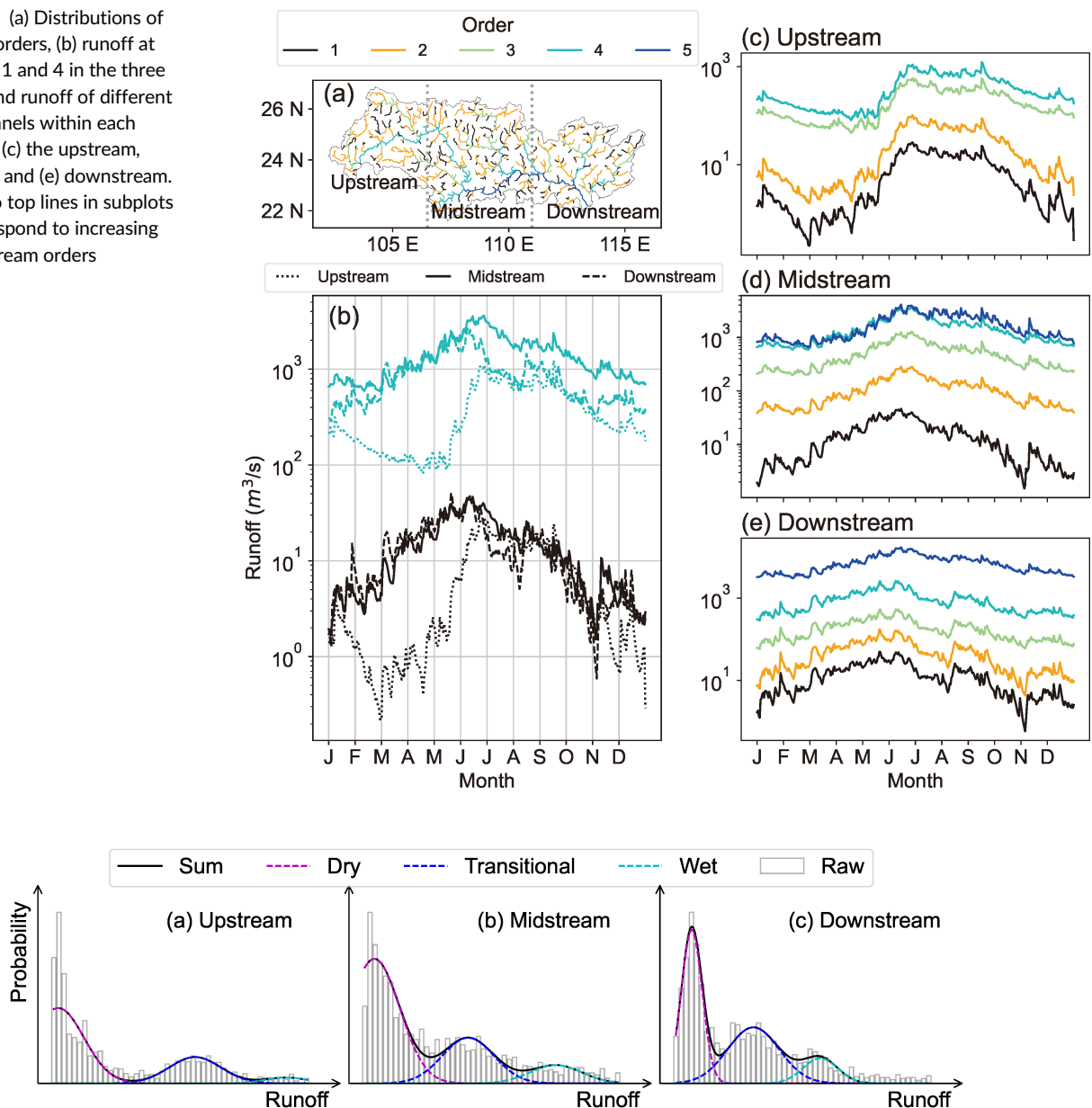

FIGURE 9 Representative probability distributions of flow in the (a) upstream, (b) midstream, and (c) downstream. Dry, Transitional, Wet, Sum, and Raw represent the decomposed modes of the dry, transitional, wet, the superposition of modes, and the raw probability distribution, respectively.

(Figures 4a, 10a). Soil properties, particularly soil texture, further influence water infiltration and soil water dynamics, leading to deviations in the spatial distribution of surface and subsurface flow from the precipitation map. Notably, regions with high rock content exhibit active aquifer flow due to high percolation rates associated with coarse textures (Figures 4c, 10c). To further quantify the impact of soil on water redistribution, we applied a threshold of 30% clay content to classify the surface soil texture into two primary groups: dense clay (>30%) and loose rocky (<30%) soil, following the USDA soil classification system.

Figure 11 shows the ratios of different flow components in various land use and soil types (Figure 11). Regarding land use roles, forested regions exhibit the highest lateral flow ratio, accounting for 24% of precipitation, while agricultural regions have a higher AET ratio (56%) compared to forests (50%) (Figure 11a). Pasture land, primarily

located in the Yungui Plateau, has the lowest total flow ratio, where AET accounted for 60% of rainfall. In urban areas, only 37% of the rain was evaporated, with the remaining water converting to surface flow, contributing to the active zone of surface flow in metropolitan areas surrounding the megacities. Wetlands converted almost one-third of precipitation into aquifer flow.

Soil influences water percolation processes. In agricultural regions with rocky soils, the aquifer flow accounts for 69% of the total flow (Figure 11b). The highest proportion of lateral flow (57%) is found in the rocky forest areas. In contrast, clay soils produce more surface flow than rocky areas. For instance, surface flow constitutes only 1% of the total flow in areas with coarse-textured soils, whereas it reaches 16% in clay soils in pasture land. In agricultural regions, aquifer flow in rocky areas accounts for 69% of the total flow, a significantly

TABLE 4 Best fit parameters of the normalized multimodal probability distribution functions (PDFs) of runoff by river orders in the three substreams.

Substream	Order	P_1	P_2	P_3	S_1	S_2	S_3	σ_1	σ_2	σ_3
Upstream	1	0.53	0.46	0.01	0.3	14.4	26.4	1.4	6.0	0.7
	2	0.56	0.40	0.04	1.7	56.3	92.2	4.1	15.0	4.0
	3	0.58	0.39	0.04	80.0	341.2	550.0	50.0	74.5	25.9
	4	0.63	0.35	0.02	110.6	704.5	1027.2	130.0	140.3	11.5
Midstream	1	0.37	0.46	0.17	3.5	15.0	33.9	1.5	5.4	5.1
	2	0.55	0.36	0.09	24.0	140.0	251.5	35.6	30.6	30.1
	3	0.57	0.34	0.09	109.8	650.0	1108.2	174.3	138.1	100.0
	4	0.63	0.24	0.13	678.4	1900.3	3016.5	407.7	200.0	500.0
	5	0.54	0.41	0.05	925.5	2500.0	3634.5	214.1	500.0	222.2
Downstream	1	0.45	0.43	0.13	3.9	15.0	28.9	2.0	5.0	3.3
	2	0.42	0.47	0.11	14.1	51.6	98.1	5.8	19.7	8.2
	3	0.44	0.35	0.21	91.6	195.2	322.0	20.1	44.3	50.0
	4	0.44	0.41	0.15	431.1	970.0	1659.6	76.5	198.9	214.6
	5	0.46	0.48	0.06	3338.1	8900.4	15597.3	1470.7	2364.7	1145.8

Note: Here, P_i, S_i, and σ_i are the representative probability, centre streamflow value, and standard deviation of the *i*th unimodal PDF, respectively.
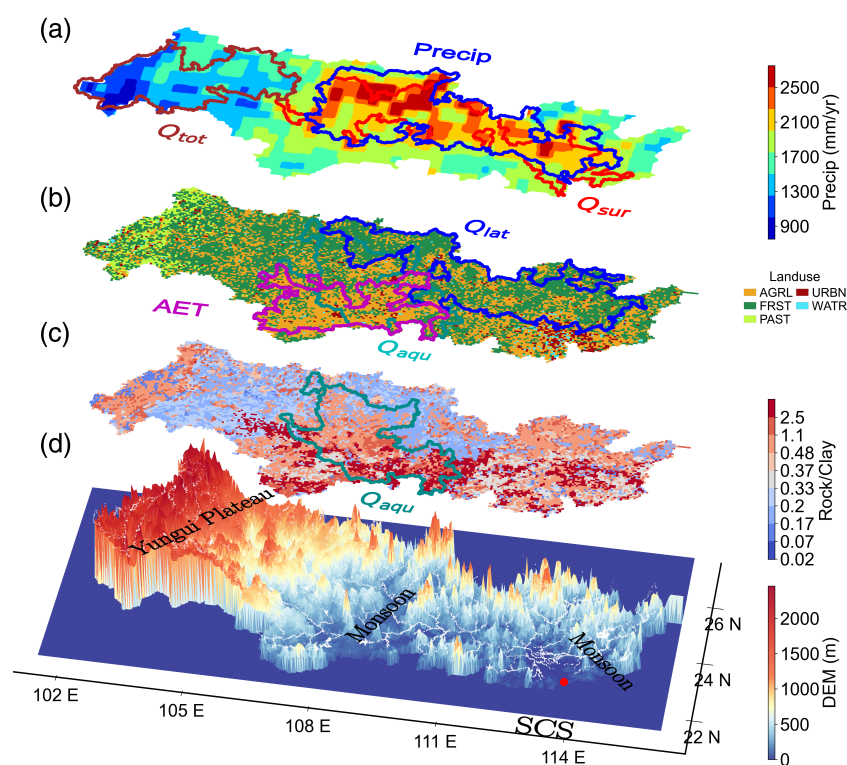

FIGURE 10 Spatial distributions of: (a) precipitation, (b) land use, (c) ratio of rock to clay (soil), and (d) topography. Coloured polygons in (a)–(c) indicate the active zones corresponding to Figure 4. AGRL, FRST, PAST, URBAN, and WATR represent agriculture, forest, pasture, urban, and water, respectively. The SCS represents the South China Sea.

higher proportion compared to soils with high clay contents, where aquifer flow accounted for 41%.

These findings highlight the intricate interplay between atmospheric and land surface properties in shaping the rainfall-runoff relationship in the PRB. The monsoon climate and topography establish the foundation for the spatial and temporal patterns of precipitation and various water fluxes. Moreover, land use and soil properties govern the conversion of precipitation into different flow components, including AET, surface flow, lateral flow, and aquifer flow.

4 | DISCUSSION

4.1 | Controls of land surface processes and atmospheric impacts

The hydrological processes in the PRB exhibit distinct seasonal patterns influenced by moisture circulation (Figure 1a). During the wet season, moisture-laden water vapours from the Bay of Bengal, the west Pacific, and the southwest side of the Tibetan Plateau play a

FIGURE 11 Ratios of flow components to (a) precipitation for different land use and (b) the total flow of dense clay and loose rocky groups. The numbers in the circles refer to percentages of flow components.
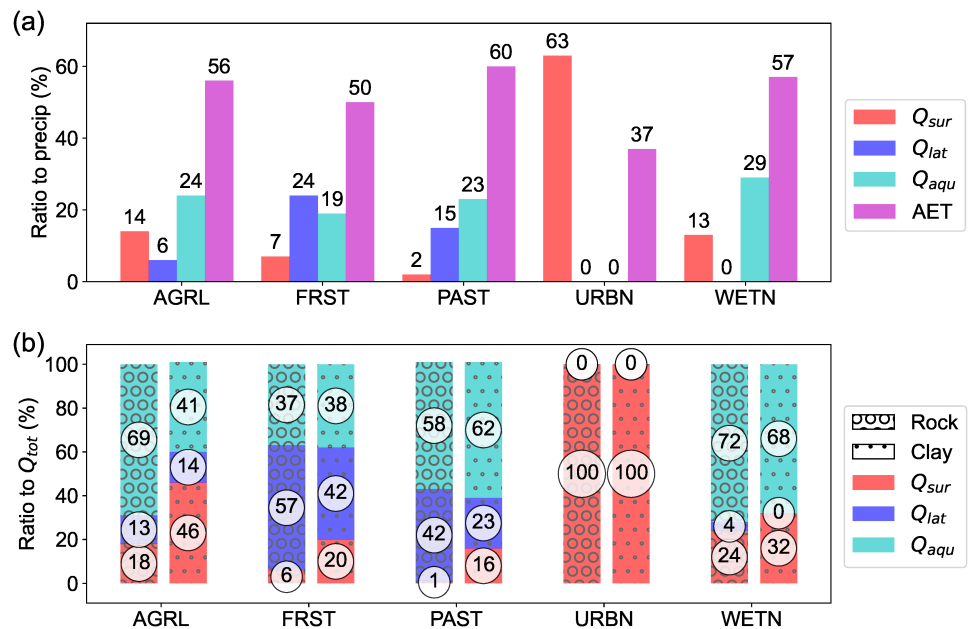
significant role in shaping the region's hydroclimate (Lu et al., 2021). The wet season encompasses the pre-flood season (April–June) and the post-flood season (July–September). The pre-flood season, accounting for nearly half of the PRB's annual precipitation (Ling, 2023), results in prolonged increased streamflow (Figures 6, 7). Moisture transport primarily occurs through the Indian Ocean channel, with a lesser contribution from the west Pacific (Shi et al., 2020). This period is characterized by two primary precipitation events: frontal heavy rainfall over inland areas and warm-sector heavy rainfall in coastal regions (Wu et al., 2020). The post-flood season, which contributes approximately 30% of the yearly rainfall, is mainly influenced by tropical cyclones moving along the southwest side of the Western Pacific Subtropical High (Li, Wang, & Lan, 2021). These cyclones suppress the moisture flux out of the PRB, resulting in short but intense rainfall and streamflow peaks in the lower substreams (Figure 7). In contrast, the streamflow in the entire basin remains low and stable during the dry seasons due to sparse precipitation (Figures 5–7). Autumn sees a decrease in moisture from the south, which further diminishes precipitation. Winter is characterized by cold and dry northeasterly winds, while the transitional spring season experiences some rainfall from the interaction of cold mainland air with warmer ocean currents (Lu et al., 2021).

The diverse topography of the PRB, ranging from coastal plains to mountainous terrains, interacts with weather systems to create spatial variability in precipitation and runoff. Coastal areas, especially the PRD in the downstream, experience heavy rainfall due to land-sea boundaries (Zhang et al., 2021). Low-level jets, associated with synoptic systems or the boundary layer, contribute to this pattern (Du & Chen, 2019). Mountainous regions such as the Nanling and Dayao mountains serve as centres for heavy precipitation, creating hydrologically active areas in the midstream subregion, which is critical for water resources management (Li, Yu, et al., 2021). These areas experience barrier effects, terrain uplift, and thermal effects of mountains

that disrupt airflow stability, enhance convective precipitation, and facilitate heavy rainfall on windward slopes. Conversely, the Yungui Plateau in the western basin receives damp Southwestern summer monsoons blocked by mountains, resulting in relatively drier conditions (Figures 7, 10). In this region, the statistical distribution of streamflow predominantly shows a dry condition (Figures 5f, 9a) during the dry seasons, highlighting the need for attention during drought events.

Land use and soil play a crucial role in controlling different components of streamflow. Natural land use types such as forests and wetlands retain more water compared to croplands and urban areas, which experience significant water loss through evapotranspiration and surface flow. The karst terrain of Guangxi province hosts the active zone of aquifer flow (Figure 4c, 10), characterized by a fractured bedrock structure and lithology that enhance water storage capacity (Zhang et al., 2007; Zhou et al., 2012). However, with projected population growth, particularly in the metropolitan region, the conversion of natural land types to croplands and urban areas is expected to continue rapidly (Chen et al., 2020). Additionally, global warming has resulted in a 10% increase in streamflow over the past half-century in the PRB, and the probability of heavy rainfall is anticipated to rise by 1.3–1.8 times in the coastal urban areas of the GBA (Hu et al., 2023). Consequently, future studies should prioritize mitigating the impacts of land conversions and climate change on flood control. Developing adaptation and mitigation strategies for a changing climate is crucial (Niu, 2013; Qiang et al., 2021).

4.2 | Uncertainties and limitations

We further evaluated our model in simulating water fluxes within the PRB by comparing it with various datasets. Our simulation shows superior time series for streamflow ($NSE = 0.9$, $RSR = 0.32$,

$Pbias = -1.3$), as depicted in Figure S9. Its efficacy surpasses that of regional models like WAPABA and meets the 'very good' level according to Moriasi et al. (2007)'s performance criteria, in contrast to national or global models such as GloFAS, GFSR, and CNRD, which only reach a 'satisfactory' level at best. The simulations also reveal consistent findings regarding runoff distribution; SWAT, GRFR, and CNRD identify active and inactive hydrological zones that align with each other (Figure S10). However, GRFR and CNRD tend to overestimate runoff in the East River Basin, indicating values exceeding 1250 mm/year. Moreover, in comparing the baseflow index with the GSCD streamflow characteristics dataset, our model shows a broader range but maintains a consistent spatial distribution (Figure S11). It is critical to recognize that different computational methods may lead to diverse baseflow index results, potentially causing discrepancies among datasets. When evaluating simulated AET flux, our model result aligns well with datasets such as GREA and GETM in spatial and temporal distributions (Figures S12 and S13), particularly mirroring GREA with a high correlation ($R^2 = 0.942$, RMSE = 6.7). For potential evapotranspiration (PET) flux (Figures S12 and S14), our spatial patterns are consistent with those of CPET, although it reports lower PET values in the southern regions, with consistent temporal variations ($R^2 = 0.794$, RMSE = 13).

Despite these alignments, uncertainties in SWAT-generated streamflow largely arise from the input meteorological dataset and the adopted model's structure. The preferred AgrEra5 forcing dataset, superior to CFSR and CMADS (see Section 2.2.2), underestimates precipitation in the coastal areas of Guangdong province where the land-sea interface promotes higher precipitation (see Section 4.1). Consequently, for smaller study areas, combining reanalysis datasets with measured data is recommended to minimize inaccuracies. The model's internal limitations, such as shortcomings in simulating flood processes and rapid streamflow fluctuations, also warrant consideration (Bieger et al., 2017). Furthermore, the model does not currently reflect the land use changes—particularly urbanization of agricultural and rural areas in recent decades (Ye et al., 2021)—which affect hydrological processes. Additionally, the impact of reservoirs, especially upstream, is significant. The residence time of 0.423 years for the entire basin, calculated by dividing the total reservoir storage capacity by the annual discharge of the Pearl River, suggests that it is necessary to incorporate detailed reservoir management into the model to improve the simulations of streamflow patterns. Model uncertainty also arises from the parameters used. Employing methods such as the Monte Carlo simulation to generate a distribution of potential streamflow outputs can assist in quantifying this uncertainty in future work. Moreover, availability of detailed data on the ratios of surface, lateral, and aquifer flows could also further enhance model calibration.

5 | CONCLUSION

The hydrological processes in the PRB exhibit significant temporal (seasonal) and spatial (zonal) variability, highlighting the influences of monsoon climate and landscape features. Based on the analysis, we draw the following conclusions:

1. The fundamental patterns of hydrological processes in the PRB are shaped by precipitation, which is influenced by the monsoon climate and terrain topography. Land use and soil texture are significant to water redistribution in the soil profile and regulate the locations of the active zones of water fluxes. The surface flow is the most active within the precipitation centres. The lateral flow and AET dominate in the forests and agricultural regions, respectively, while the aquifer flow is more active in areas with coarse soil textures.

2. All hydrological processes in the PRB exhibit significant spatiotemporal variability. AET and aquifer retention cause the streamflow and precipitation to be out-of-phase. The surface/aquifer flow displays the strongest/weakest variations in space and time, while the lateral flow varies at an intermediate level between the surface and aquifer flows.

3. Based on the hydrological variability, the PRB can be divided into three substreams: a drought-prone upstream, a hydrologically active midstream, and a typhoon-affected downstream from west to east. Streamflow within each substream is interconnected and exhibits similar temporal patterns and statistical distributions.

4. The streamflow PDFs are multimodal, and the PDFs can be decomposed into three unimodal distributions representing dry, transitional, and wet conditions. The PRB features a large and steep dry mode, a flat transitional mode, and a short wet mode. The percentages and centre values of each mode vary among the substream subregions, reflecting the diverse dynamics of water resources within each substream.

CONFLICT OF INTEREST STATEMENT

The authors declare that they have no known competing financial interests or personal relationships that could have appeared to influence the work reported in this paper.

DATA AVAILABILITY STATEMENT

The data that support the findings of this study are available from the corresponding author upon reasonable request.

ORCID

Ying Zhang https://orcid.org/0000-0002-8126-7000

REFERENCES

Arnold, J. G., Moriasi, D., Gassman, P., Abbaspour, K., White, M., Srinivasan, R., Santhi, C., Harmel, R., van Griensven, A., Van Liew, M., Kannan, N., & Jha, M. (2012). SWAT: Model Use, Calibration, and Validation. *Transactions of the ASABE*, *55*(4), 1491–1508. https://doi.org/10.13031/2013.42256

Arnold, J. G., Srinivasan, R., Muttiah, R. S., & Williams, J. R. (1998). Large area hydrologic modeling and assessment part I: Model development I. *Journal of the American Water Resources Association*, *34*, 73–89.

Bell, E. F., Wolf, C., Meisenheimer, K., Rix, H.-W., Borch, A., Dye, S., Kleinheinrich, M., Wisotzki, L., & McIntosh, D. H. (2004). Nearly 5000 distant early-type galaxies in COMBO-17: A red sequence and its evolution since ∼1. *The Astrophysical Journal*, *608*, 752–767.

Bieger, K., Arnold, J. G., Rathjens, H., White, M. J., Bosch, D. D., Allen, P. M., Volk, M., & Srinivasan, R. (2017). Introduction to SWAT+, a completely restructured version of the soil and water assessment tool. *Journal of the American Water Resources Association*, *53*, 115–130.

Bossa, A. Y., Diekkrüger, B., Igué, A. M., & Gaiser, T. (2012). Analyzing the effects of different soil databases on modeling of hydrological processes and sediment yield in Benin (West Africa). *Geoderma*, *173-174*, 61–74.

Bullock, A., & Acreman, M. (2003). The role of wetlands in the hydrological cycle. *Hydrology and Earth System Sciences*, *7*, 358–389.

Chen, M., Vernon, C. R., Graham, N. T., Hejazi, M., Huang, M., Cheng, Y., & Calvin, K. (2020). Global land use for 2015–2100 at 0.05° resolution under diverse socioeconomic and climate scenarios. *Scientific Data*, *7*, 320. https://doi.org/10.1038/s41597-020-00669-x

Dai, C., Liu, Y., Wang, T., Li, Z., & Zhou, Y. (2018). Exploring optimal measures to reduce soil erosion and nutrient losses in southern China. *Agricultural Water Management*, *210*, 41–48. https://doi.org/10.1016/j.agwat.2018.07.032

Deng, Y., Duan, X., Ding, S., Cai, C., & Chen, J. (2018). Suction stress characteristics in granite red soils and their relationship with the collapsing gully in south China. *Catena*, *171*, 505–522.

Du, Y., & Chen, G. (2019). Heavy rainfall associated with double low-level jets over southern China. Part II: Convection initiation. *Monthly Weather Review*, *147*, 543–565. https://doi.org/10.1175/MWR-D-18-0102.1

Eckhardt, K. (2005). How to construct recursive digital filters for baseflow separation. *Hydrological Processes*, *19*, 507–515.

Fu, B., Merritt, W. S., Croke, B. F. W., Weber, T. R., & Jakeman, A. J. (2019). A review of catchment-scale water quality and erosion models and a synthesis of future prospects. *Environmental Modelling and Software*, *114*, 75–97.

Gao, Z., Niu, F., Lin, Z., & Luo, J. (2021). Fractal and multifractal analysis of soil particle-size distribution and correlation with soil hydrological properties in active layer of Qinghai–Tibet plateau, China. *Catena*, *203*, 105373. https://doi.org/10.1016/j.catena.2021.105373

Giri, S., Arbab, N. N., & Lathrop, R. G. (2018). Water security assessment of current and future scenarios through an integrated modeling framework in the Neshanic River watershed. *Journal of Hydrology*, *563*, 1025–1041.

Hu, C., Tam, C.-Y., Li, X., Huang, K., Ren, C., Fung, K. Y., & Wang, Z. (2023). Mega-city development impact on hourly extreme rainfall over the South China Greater Bay Area under near-future climate warming. *Urban Climate*, *48*, 101389. https://doi.org/10.1016/j.uclim.2022.101389

Knoben, W. J. M., Woods, R. A., & Freer, J. E. (2018). A quantitative hydrological climate classification evaluated with independent streamflow data. *Water Resources Research*, *54*, 5088–5109. https://doi.org/10.1029/2018WR022913

Lee, B. J., Fettweis, M., Toorman, E., & Molz, F. J. (2012). Multimodality of a particle size distribution of cohesive suspended particulate matters in a coastal zone. *Journal of Geophysical Research: Oceans*, *117*, C03014.

Li, G., Yu, Z., Wang, W., Ju, Q., & Chen, X. (2021). Analysis of the spatial distribution of precipitation and topography with GPM data in the Tibetan plateau. *Atmospheric Research*, *247*, 105259. https://doi.org/10.1016/j.atmosres.2020.105259

Li, X., Wang, C., & Lan, J. (2021). Role of the South China Sea in southern China rainfall: Meridional moisture flux transport. *Climate Dynamics*, *56*, 2551–2568. https://doi.org/10.1007/s00382-020-05603-w

Lin, H. (2012). Hydropedology: Summary and outlook-chapter 24. *Hydropedology* (pp. 759–781). Elsevier.

Ling, G. (2023). Comparing water vapor transport during precipitation processes in the pre-flood period of South China and precipitation processes of typhoons in the post-flood period of South China: A case study. *Dynamics of Atmospheres and Oceans*, *102*, 101371. https://doi.org/10.1016/j.dynatmoce.2023.101371

Liu, Z., Xie, Y., Cheng, L., Lin, K., Tu, X., & Chen, X. (2021). Stability of spatial dependence structure of extreme precipitation and the concurrent risk over a nested basin. *Journal of Hydrology*, *602*, 126766. https://doi.org/10.1016/j.jhydrol.2021.126766

Lu, X., Li, Q., Zhao, W., Xiao, A., Li, G., & Yu, Z. (2021). Spatiotemporal characteristics of rainfall in South China from 1967 to 2018. *Journal of Applied Meteorology and Climatology*, *60*, 1333–1345. https://doi.org/10.1175/JAMC-D-20-0191.1

Ly, K., Metternicht, G., & Marshall, L. (2019). Transboundary river catchment areas of developing countries: Potential and limitations of watershed models for the simulation of sediment and nutrient loads. A review. *Journal of Hydrology: Regional Studies*, *24*, 100605.

Moriasi, D. N., Arnold, J. G., Liew, M. W., Bingner, R. L., Harmel, R. D., & Veith, T. L. (2007). Model evaluation guidelines for systematic quantification of accuracy in watershed simulations. *Transactions of the ASABE*, *50*, 885–900.

Niu, J. (2010). Terrestrial hydrological features of the Pearl River basin in South China. *Journal of Hydro-environment Research*, *4*(4), 279–288.

Niu, J. (2013). Precipitation in the Pearl River basin, South China: Scaling, regional patterns, and influence of large-scale climate anomalies. *Stochastic Environmental Research and Risk Assessment*, *27*, 1253–1268. https://doi.org/10.1007/s00477-012-0661-2

Niu, J., Chen, J., & Sivakumar, B. (2014). Teleconnection analysis of runoff and soil moisture over the Pearl River basin in southern China. *Hydrology and Earth System Sciences*, *18*, 1475–1492.

Niu, J., Chen, J., & Sun, L. (2015). Exploration of drought evolution using numerical simulations over the Xijiang (West River) basin in South China. *Journal of Hydrology*, *526*, 68–77. https://doi.org/10.1016/j.jhydrol.2014.11.029

Niu, J., Chen, J., Wang, K., & Sivakumar, B. (2017). Coherent modes in multi-scale variability of precipitation over the headwater catchments in the Pearl River basin, South China. *Hydrological Processes*, *31*, 948–955.

PRWRC. (2021). Pearl River water resources bulletin. *Pearl River Water Resources Commission*, *25*, 2000–2021. (in Chinese).

Qiang, Y., Zhang, L., He, J., Xiao, T., Huang, H., & Wang, H. (2021). Urban flood analysis for Pearl River Delta cities using an equivalent drainage method upon combined rainfall-high tide-storm surge events. *Journal of Hydrology*, *597*, 126293.

Ren, D., Engel, B., Mercado, J. A. V., Guo, T., Liu, Y., & Huang, G. (2022). Modeling and assessing water and nutrient balances in a tile-drained agricultural watershed in the U.S. Corn Belt. *Water Research*, *210*, 117976. https://doi.org/10.1016/j.watres.2021.117976

Ribolzi, O., Lacombe, G., Pierret, A., Robain, H., Sounyafong, P., de Rouw, A., Soulileuth, B., Mouche, E., Huon, S., Silvera, N., Latxachak, K., Sengtaheuanghoung, O., & Valentin, C. (2018). Interacting land use and soil surface dynamics control groundwater outflow in

a montane catchment of the lower Mekong basin. *Agriculture, Ecosystems and Environment*, 268, 90–102. https://doi.org/10.1016/j.agee.2018.09.005

Sah, R. K., & Das, A. K. (2017). Minimizing ambiguities in stream classification of complex drainage structures. *Journal of Hydrology*, 553, 224–230.

Shanyavskiy, A. A., & Soldatenkov, A. P. (2019). The fatigue limit of metals as a characteristic of the multimodal fatigue life distribution for structural materials. *Procedia Structural Integrity*, 23, 63–68.

Shi, Y., Jiang, Z., Liu, Z., & Li, L. (2020). A Lagrangian analysis of water vapor sources and pathways for precipitation in East China in different stages of the east Asian summer monsoon. *Journal of Climate*, 33, 977–992. https://doi.org/10.1175/JCLI-D-19-0089.1

Shukla, S., & Wood, A. W. (2008). Use of a standardized runoff index for characterizing hydrologic drought. *Geophysical Research Letters*, 35(2), L02405. https://doi.org/10.1029/2007GL032487

Shuler, C. K., Dulai, H., Leta, O. T., Fackrell, J., Welch, E., & El-Kadi, A. I. (2020). Understanding surface water–groundwater interaction, submarine groundwater discharge, and associated nutrient loading in a small tropical Island watershed. *Journal of Hydrology*, 585, 124342.

Strahler, A. N. (1957). Quantitative analysis of watershed geomorphology. *Transactions, American Geophysical Union*, 38, 913–920.

Tarboton, D. G., Bras, R. L., & Rodriguez-Iturbe, I. (1991). On the extraction of channel networks from digital elevation data. *Hydrological Processes*, 5, 81–100.

Veettil, A. V., & Mishra, A. K. (2016). Water security assessment using blue and green water footprint concepts. *Journal of Hydrology*, 542, 589–602.

Wang, C., Shang, S., Jia, D., Han, Y., Sauvage, S., Sánchez-Pérez, J.-M., Kuramochi, K., & Hatano, R. (2018). Integrated effects of land use and topography on streamflow response to precipitation in an agriculture-forest dominated northern watershed. *Water*, 10, 633. https://doi.org/10.3390/w10050633

Wu, K., & Xu, Y. J. (2006). Evaluation of the applicability of the SWAT model for coastal watersheds in southeastern Louisiana. *Journal of the American Water Resources Association*, 42, 1247–1260. https://doi.org/10.1111/j.1752-1688.2006.tb05610.x

Wu, N., Ding, X., Wen, Z., Chen, G., Meng, Z., Lin, L., & Min, J. (2020). Contrasting frontal and warm-sector heavy rainfalls over South China during the early-summer rainy season. *Atmospheric Research*, 235, 104693. https://doi.org/10.1016/j.atmosres.2019.104693

Wu, S., Zhao, J., Wang, H., & Sivapalan, M. (2021). Regional patterns and physical controls of streamflow generation across the conterminous United States. *Water Resources Research*, 57, e2020WR028086. https://doi.org/10.1029/2020WR028086

Wu, T., Zhu, L.-J., Shen, S., Zhu, A. X., Shi, M., & Qin, C.-Z. (2023). Identification of watershed priority management areas based on landscape positions: An implementation using SWAT+. *Journal of Hydrology*, 619, 129281. https://doi.org/10.1016/j.jhydrol.2023.129281

Yamamoto, T., Malingin, M., Pepino, M. M., Yoshikai, M., Campos, W., Miyajima, T., Watanabe, A., Tanaka, Y., Morimoto, N., Ramos, R., Pagkalinawan, H., & Nadaoka, K. (2019). Assessment of coastal turbidity improvement potential by terrigenous sediment load reduction and its implications on seagrass inhabitable area in Banate Bay, central Philippines. *The Science of the Total Environment*, 656, 1386–1400.

Yan, R., Zhang, X., Yan, S., Zhang, J., & Chen, H. (2018). Spatial patterns of hydrological responses to land use/cover change in a catchment on the loess plateau, China. *Ecological Indicators*, 92, 151–160. https://doi.org/10.1016/j.ecolind.2017.04.013

Yang, Q., Almendinger, J. E., Zhang, X., Huang, M., Chen, X., Leng, G., Zhou, Y., Zhao, K., Asrar, G. R., Srinivasan, R., & Li, X. (2018). Enhancing SWAT simulation of forest ecosystems for water resource assessment: A case study in the St. Croix River basin. *Ecological Engineering*, 120, 422–431. https://doi.org/10.1016/j.ecoleng.2018.06.020

Yang, T., Shao, Q., Hao, Z.-C., Chen, X., Zhang, Z., Xu, C.-Y., & Sun, L. (2010). Regional frequency analysis and spatio-temporal pattern characterization of rainfall extremes in the Pearl River Basin, China. *Journal of Hydrology*, 380, 386–405.

Ye, Y., Zhang, J., Wang, T., Bai, H., Wang, X., & Zhao, W. (2021). Changes in land-use and ecosystem service value in Guangdong Province, southern China, from 1990 to 2018. *Landscape*, 10, 426. https://doi.org/10.3390/land10040426

Yu, S., Bond, N. R., Bunn, S. E., Xu, Z., & Kennard, M. J. (2018). Quantifying spatial and temporal patterns of flow intermittency using spatially contiguous runoff data. *Journal of Hydrology*, 559, 861–872. https://doi.org/10.1016/j.jhydrol.2018.03.009

Zeiger, S. J., Owen, M. R., & Pavlowsky, R. T. (2021). Simulating nonpoint source pollutant loading in a karst basin: A SWAT modeling application. *Science of the Total Environment*, 785, 147295. https://doi.org/10.1016/j.scitotenv.2021.147295

Zhang, C., Huang, X., Fei, J., Luo, X., & Zhou, Y. (2021). Spatiotemporal characteristics and associated synoptic patterns of extremely persistent heavy rainfall in southern China. *Journal of Geophysical Research: Atmospheres*, 126, e2020JD033253. https://doi.org/10.1029/2020JD033253

Zhang, H., Wang, B., Liu, D. L., Zhang, M., Leslie, L. M., & Yu, Q. (2020). Using an improved SWAT model to simulate hydrological responses to land use change: A case study of a catchment in tropical Australia. *Journal of Hydrology*, 585, 124822.

Zhang, Q., Gu, X., Singh, P. V., Xiao, M., & Xu, C. (2014). Stationarity of annual flood peaks during 1951–2010 in the Pearl River basin, China. *Journal of Hydrology*, 519, 3263–3274. https://doi.org/10.1016/j.jhydrol.2014.10.028

Zhang, Q., Xiao, M., Singh, V. P., & Li, J. (2012). Regionalization and spatial changing properties of droughts across the Pearl River basin, China. *Journal of Hydrology*, 472-473, 355–366.

Zhang, Q., Xu, C.-Y., & Zhang, Z. (2009). Observed changes of drought/wetness episodes in the Pearl River basin, China, using the standardized precipitation index and aridity index. *Theoretical and Applied Climatology*, 98, 89–99.

Zhang, S., Lu, X. X., Higgitt, D. L., Chen, C.-T. A., Sun, H.-G., & Han, J.-T. (2007). Water chemistry of the Zhujiang (Pearl River): Natural processes and anthropogenic influences. *Journal of Geophysical Research: Earth Surface*, 112, F01011. https://doi.org/10.1029/2006JF000493

Zhou, R., Guo, C., Fu, Q., & Pan, L. (2012). Study on the drought and flood disasters formation mechanism in karst regions of middle Guangxi. *Procedia Engineering*, 28, 277–281. https://doi.org/10.1016/j.proeng.2012.01.719

Zhou, Z., Shi, H., Fu, Q., Ding, Y., Li, T., Wang, Y., & Liu, S. (2021). Characteristics of propagation from meteorological drought to hydrological drought in the Pearl River Basin. *Journal of Geophysical Research: Atmospheres*, 126, e2020JD033959. https://doi.org/10.1029/2020JD033959

SUPPORTING INFORMATION

Additional supporting information can be found online in the Supporting Information section at the end of this article.

How to cite this article: Zhang, Y., Gan, J., & Yang, Q. (2024). Spatiotemporal variability of streamflow in the Pearl River Basin: Controls of land surface processes and atmospheric impacts. *Hydrological Processes*, 38(4), e15151. https://doi.org/10.1002/hyp.15151